https://doi.org/10.1016/j.apacoust.2020.107382

Acoustic Silencing in a Flow Duct with Micro-Perforated Panel Liners

Xiaoqi Zhang and Li Cheng*

Department of Mechanical Engineering, The Hong Kong Polytechnic University, Kowloon, Hong Kong, China

* Corresponding author.
Email address: li.cheng@polyu.edu.hk

Abstract

Despite the increasing interest in Micro-perforated panels (MPPs) for various noise control applications, the acoustic behavior of MPP liners in flow ducts has not been fully apprehended. On the top of this is the lack of understanding on the influence of various design arrangements and system parameters on the performance of MPP-based acoustic silencing devices. Incorporating previously developed acoustic impedance formulae within the general framework of the Patch Transfer Function (PTF) framework, these issues are investigated in this paper in the context of a MPP liner, flush-mounted inside a flow duct wall. Numerical analyses reveal the effects of the grazing flow and different partition arrangements in the backing cavity of MPP liners on their silencing performance as well as the underlying physical phenomena. Capitalizing on the efficiency of the modelling approach, a system optimization is carried out. The numerically predicted noise attenuation results are validated through comparisons with experimental measurements under various grazing flow velocities. While shedding light on the underlying sound attenuation mechanism, studies provide guidelines for the design of MPP silencers in flow ducts.

1. Introduction

Micro-perforated panels (MPPs) take the form of thin sheets with perforated thickness-through holes, typically sized in the sub-millimeter range. With holes in such a small scale, the panels alone can provide a high acoustic resistance and a low acoustic reactance, conducive to effective sound absorption without the use of any porous materials. Upon a proper design, broadband noise absorption can be achieved. Owing to their lightweight, fibrous-free and environmental friendly features, MPPs are widely used as sound absorbers in many engineering applications, such as in room acoustic problems [1-5], environmental noise abatement [6, 7] as well as noise control of compact mechanical systems [8-11]. Relevent issues related to MPP designs have been extensively investigated in order to improve the sound absorptions in various noise control cicumstances [12-15].

As an important application, MPPs are widely used in silencer design for duct noise suppressions. Early attempts to use MPPs as liners in a duct were reported, exemplified by the work of Wu [16], in which the acoustic performance of a MPP liner was investigated with grazing flow using theoretically derived sound attenuation prediction equations. However, limited by the assumptions made in the study, the prediction results only qualitatively agree with experiments and the discussions on the effects of silencer geometric parameters are restricted to the locally reacting case only. More recently, Allam and Abom [17, 18] investigated MPP silencers with grazing flow and

showed the effect of the partition inside the backing cavity and that of the grazing flow without particular focus on other MPP geometrical parameters. Wang *et al.* [19] proposed a hybrid and non-locally reacting silencer, dissipative and reactive, consisting of an expansion chamber with two side-branch cavities covered by two light and moderately stiff MPPs, and demonstrated that a wider acoustic attenuation bandwidth could be achieved with MPPs compared to a flexible plate without micro-perforations. Shi *et al.* [20] investigated the acoustic attenuation of a periodically arranged array of micro-perforated tube mufflers and found that, by selecting an appropriate periodic distance, the MPP silencers can be tuned to control low frequency noise within a broader frequency range. Yu *et al.*[21] studied the hybrid noise attenuation mechanism of MPP silencers and analyzed the possible influences of the system parameters, without however considering the grazing flow effects like many other investigations reported in the open literature [19, 20, 22].

Existing works allowed revealing useful physical insights to guide the design of MPP silencers for duct noise control. While cases without flow [19-22] have been extensively studied using classical acoustic impedance formulae proposed by Maa [23], research on MPPs in ducts with grazing flow effects is fairly limited, with the exception of a very small number of papers [16-18]. In addition, while one gets a resealable understanding on some influencing system parameters such as solid partition arrangements in the backing cavity behind the MPPs [17, 21, 24], possibilities of exploring these effects for possible optimal design of MPP silencers have not been fully

explored in the literature. One of the plausible reasons is that the presence of flow inside a duct poses significant challenges in terms of both MPP characterization and system modelling. For the former, as previously reviewed [25], fundamental issues like the realistic prediction of acoustic impedance of MPPs in the presence of flow has long been a bottle-necking problem. This is obviously due to the complex interaction between the acoustic waves and the flow field within and in the vicinity of the MPP holes. Meanwhile, a MPP liner in a flow duct is surrounded by a complex acoustic environment so that its coupling with the acoustic filed in both the duct and the backing cavity needs to be considered. This again is a very challenging task. Previous research [21] shows that the acoustic behavior of MPPs are sensitive to various system parameters and optimizations are needed to achieve an optimal design, which increases the level of difficulties when using conventional modeling techniques. For example, one dimensional modeling techniques [16] can hardly characterize these coupling effects and limited to low-order acoustic mode propagation, while techniques like modal approach with interface matching technique [26, 27] or finite element method (FEM) [17] would become very tedious when one needs to tune system parameters or to cope with the increasing system complexity and the evolving system configuration during system optimization. Consequently, there is a need to seek more efficient and flexible prediction tools for the design and optimization of MPP silencers.

Motivated by this and capitalizing on the previously established acoustic impedance prediction tool detailed in Ref. [25], a subsystem modelling technique,

referred to as Patch Transfer Function approach (PTF) [21], is revamped and used to tackle the aforementioned numerical challenges, in the context of MPP liners in a flow duct. Through numerical simulations and analyses, issues like the effect of the grazing flow and that of different partition arrangements in the backing cavity of MPP liners on their silencing performance and optimization, as well as the underlying physical phenomena, are scrutinized, aiming at providing practical guidelines for their design.

The rest of the paper is organized as follows. After a brief recap of its principle, PTF formulation is presented and implemented on MPP silencers with and without grazing flow. The established PTF model is then experimentally validated. Numerical analyses are then carried out to show the effects of various system parameters on the acoustic behavior of MPP silencers alongside discussions on the underlying physics relating to the different MPP backing arrangements. Finally, system optimizations are performed to show the capability of the proposed model in coping with the system complexity and in obtaining the best possible noise attenuation performance within a prescribed frequency range.

2. Formulation of the flow duct problem

The system under investigation is illustrated in Fig. 1. A MPP, backed by an acoustic cavity, is flush-mounted on the wall of a flow duct with a rectangular cross section. The Patch Transfer Function (PTF) approach is employed to model the system . The study is limited to low speed flow cases. Therefore, the grazing flow effects are

only incorporated into the acoustic impedance of MPPs and the convective effects of the flow on the wave propagation in the duct are neglected [17].

The underlying principle of the PTF method is briefly recapped for the completeness of the paper. As a sub-structuring modelling approach [28], the PTF method first partitions the global system into subsystems. The interface between each pair of adjacent subsystems, called coupling surface, is then segmented into small elements, called patches. These coupling interfaces are considered to be flexible. The patches are considered as the vibrating boundary of the corresponding subsystem, thus transmitting energy from one subsystem to the other once they are coupled together. Previous studies [9, 28, 29] have shown that when the size of the patch is smaller than the half wavelength of the highest frequency of interest, the pressure or velocity at any given point on the patch can be reasonably approximated by the space-averaged pressure or velocity over the patch. Considering this, the acoustic field in each subsystem can then be coupled together through patch-based interface matching technique by ensuring the dynamic balance of the mean pressure and the continuity of the normal velocity across each patch.

The aforementioned modelling principle is implemented on the flow duct system. The whole system is divided into five subsystems, namely, an inlet duct, a main cavity, an outlet duct, a MPP and a side branch cavity, separated by the coupling surfaces C1, C2 and C3, as shown in Fig. 2. Each side of a coupling surface belongs to a different

subsystem. Taking the coupling surface C3, occupied by the MPP, as an example, its upper side, donated by MC_3, belongs to the main cavity while the lower side SC_3 to the side branch cavity. Each coupling surface is then meshed into patches, according to the half-wavelength rule [9, 28, 29].

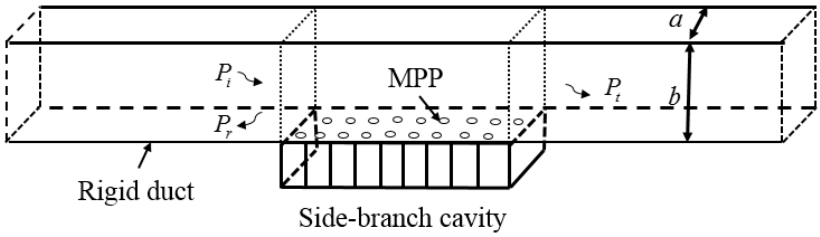

Figure 1. Sketch of the investigated flow duct system.

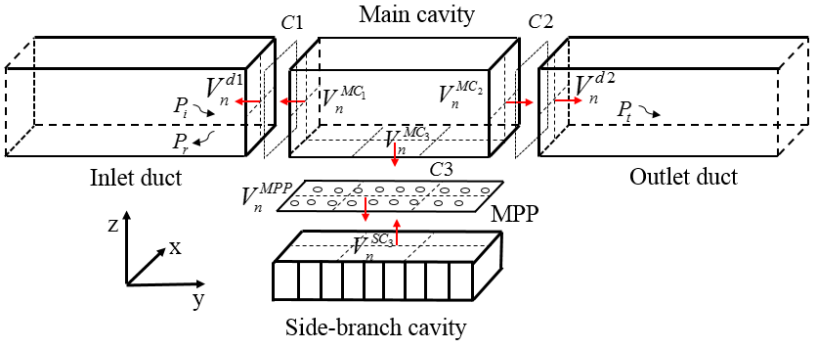

Figure 2. Sub-system treatment used in PTF modelling and definition of interfaces.

Before coupling them together, each sub-system needs to be *a priori* characterized separately. This is achieved by calculating the so-called transfer functions between different patches, called patch transfer functions (PTFs). The PTFs describe the relationship between the response on a receiving patch and the excitation on an excited

patch, be it for an acoustic subsystem or a vibrating subsystem.

For a mechanical vibrating interface, the PTFs are defined as the ratio of the mean velocity on a receiving patch over the mean force applied on an excitation patch, equivalent to patch structural mobility, written as,

$$Y_{re} = \frac{\overline{u}_r}{\overline{f}_e} \tag{1}$$

where $\overline{u}_r = \frac{1}{S_r}\int_{S_r} u_{x,y,z} dS$ is the mean normal velocity on the receiving patch r resulted from the mean normal force excitation $\overline{f}_e = \frac{1}{S_e}\int_{S_e} f_{x,y,z} dS$ exerted on the excited patch e, with S_r and S_e being the surface area of the receiving and excited patches, respectively.

For an acoustic coupling surface, a mean normal velocity $\overline{u}_e = \frac{1}{S_e}\int_{Se} u_{x,y,z} dS$ imposed on patch e generates a mean acoustic pressure on the receiving patch r, $\overline{p}_r = \frac{1}{S_r}\int_{S_r} p_{x,y,z} dS$. The PTF between the two patches is then defined as,

$$Z_{re} = \frac{\overline{p}_r}{\overline{u}_e} \tag{2}$$

When the two adjacent sub-systems are coupled together, the mean acoustic pressure on each patch is the sum of the pressure resulted from the vibrations of all

patches and from the external pressure $\overline{p}_r^{\sim}$ in the subsystem before coupling. Assuming the linearity of the system, the mean pressure on one patch writes:

$$\overline{p}_r = \overline{p}_r^{\sim} + \sum_{e=1}^{N_a} Z_{re}\overline{u}_e\,, \quad \forall r \in [1,...,N_a] \tag{3}$$

where N_a is the number of patches in an acoustic sub-system.

Similarly, the normal force exerted on one patch of a vibrating structure interface can result in the vibration of the patch itself and all other patches on the interface. Owing to the linearity of the system, the mean normal velocity of the patch is thus the sum of the velocities induced by the force exerted on all patches on the interface and the velocity $\overline{u}_r^{\sim}$ due to the mechanical force exerted on this patch before coupling, which writes

$$\overline{u}_r = \overline{u}_r^{\sim} + \sum_{e=1}^{N_V} Y_{re}\,\overline{f}_e\,, \quad \forall r \in [1,...,N] \tag{4}$$

where N_V is the number of patches over the vibrating interface.

After applying the continuity condition on the connecting patches of the three coupling surfaces, *C1* to *C3*, namely the force balance of each patch and the equality of the normal velocity, the five divided individual subsystems can be coupled together, yielding:

$$\overline{p}_1^{\sim d1} + \sum_{e}^{N_1} Z_{re}^{d1d1}\overline{u}_e^{d1} = \sum_{e}^{N_1} Z_{re}^{MC_1MC_1}\overline{u}_e^{MC_1} + \sum_{e}^{N_2} Z_{re}^{MC_1MC_2}\overline{u}_e^{MC_2} + \sum_{e}^{N_3} Z_{re}^{MC_1MC_3}\overline{u}_e^{MC_3}$$

$\forall r \in [1,...,N_1]$ at C1

$$\sum_{e}^{N_2} Z_{re}^{d2d2} \bar{u}_e^{d2} = \sum_{e}^{N_1} Z_{re}^{MC_2MC_1} \bar{u}_e^{MC_1} + \sum_{e}^{N_2} Z_{re}^{MC_2MC_2} \bar{u}_e^{MC_2} + \sum_{e}^{N_3} Z_{re}^{MC_2MC_3} \bar{u}_e^{MC_3}$$

$\forall r \in [1,...,N_2]$ at C2

$$\sum_{e}^{N_3} Y_{re}^{MPP} S_e \left(\sum_{j}^{N_1} Z_{ej}^{MC_3MC_1} \bar{u}_j^{MC_1} + \sum_{j}^{N_2} Z_{ej}^{MC_3MC_2} \bar{u}_j^{MC_2} + \sum_{j}^{N_3} Z_{ej}^{MC_3MC_3} \bar{u}_e^{MC_3} - \sum_{j}^{N_3} Z_{ej}^{SC_3SC_3} \bar{u}_j^{SC_3}\right) = \bar{u}_r^{MPP}$$

$\forall r \in [1,...,N_3]$ at C3 (5)

where N_1, N_2 and N_3 are the total number of patches at the three coupling interfaces, respectively.

The equality of the normal velocity on each side of the patches at the three coupling interfaces writes:

$$\bar{u}_{n_1}^{d1} = \bar{u}_{n_1}^{MC_1} \quad \forall n_1 \in [1,...,N_1] \text{ at C1}$$

$$\bar{u}_{n_2}^{d2} = \bar{u}_{n_2}^{MC_2} \ \forall n_2 \in [1,...,N_2] \text{ at C2}$$

$$\bar{u}_{n_3}^{MC_3} = \bar{u}_{n_3}^{MPP} = -\bar{u}_{n_3}^{SC_3} \ \forall n_3 \in [1,...,N_3] \text{ at C3} \quad (6)$$

The above equations can then be combined in the following condensed matrix form:

$$P^{\sim d_1} + Z^{d1d1} V_n^{d1} = Z^{MC_1MC_1} V_n^{MC_1} + Z^{MC_1MC_2} V_n^{MC_2} + Z^{MC_1MC_3} V_n^{MC_3}$$

$$Z^{d2d2} V_n^{d2} = Z^{MC_2MC_1} V_n^{MC_1} + Z^{MC_2MC_2} V_n^{MC_2} + Z^{MC_2MC_3} V_n^{MC_3}$$

$$Y^{MPP} S_e \left(Z^{MC_3MC_1} V_n^{MC_1} + Z^{MC_3MC_2} V_n^{MC_2} + Z^{MC_3MC_3} V_n^{MC_3} - Z^{SC_3SC_3} V_n^{SC_3}\right) = V_n^{MPP}$$

$$V_n^{MC_1} = V_n^{d1}$$

$$V_n^{MC_2} = V_n^{d2}$$

$$V_n^{MC_3} = V_n^{MPP} = -V_n^{SC_3} \quad (7)$$

Equation 7 can be further condensed into the following form,

$$\{Z\}\{V\}=\{F\} \tag{8}$$

where $Z=\begin{bmatrix} Z^{MC_1MC_1}-Z^{d1d1} & Z^{MC_1MC_2} & Z^{MC_1MC_3} \\ Z^{MC_2MC_1} & Z^{MC_2MC_1}-Z^{d2d2} & Z^{MC_2MC_3} \\ Y^{MPP}S_eZ^{MC_3MC_1} & Y^{MPP}S_eZ^{MC_3MC_2} & Y^{MPP}S_e(Z^{MC_3MC_3}+Z^{SC_3SC_3})-I \end{bmatrix}$,

$V=\begin{bmatrix} V_n^{MC_1} \\ V_n^{MC_2} \\ V_n^{MC_3} \end{bmatrix}$ and $F=\begin{bmatrix} P^{\sim d_1} \\ 0 \\ 0 \end{bmatrix}$.

The derivation of the equations used to calculate the PTFs of the subsystems like the duct, the main cavity and the side branch cavity without partition are rather straightforward due to their simple geometry [21]. Corresponding formulae of these PTFs are only briefly summarized here for convenience. Note that the defined directions of the normal velocities of these subsystems are shown in Fig. 2.

Both the main cavity and the side branch cavity without partition can be modeled as a 3D rectangular cavity. Based on the classical mode-decomposition theory and making use of the Green's function with Helmholtz equation, the PTF between patches is obtained as

$$Z_{re}^{C}=\frac{\bar{p}_r}{\bar{u}_e}=\sum_i \frac{j\omega\rho_0c^2}{\Lambda_i(\omega^2-\omega_i^{\,2})S_r}\int_{S_r}\varphi_i dS_r\int_{Se}\varphi_i dS_e \tag{9}$$

where ρ_0 is the air density; c the sound speed in the air; ω the angular frequency; $\Lambda_i=\int_{V_c}\varphi_i^2 dV_c$ with V_c being the volume of the cavity and φ_i the i th rigid-walled acoustic mode shape function, analytically expressed as

$$\varphi_i(x,y,z)=\cos\left(\frac{p\pi}{Lx}x\right)\cos\left(\frac{q\pi}{Ly}y\right)\cos\left(\frac{r\pi}{Lz}z\right)\quad p,q,r=0,1,2..... \tag{10}$$

where L_x, L_y and L_z are the side lengths of the cavity

The rectangular inlet and outlet ducts can be modeled as a semi-infinite duct with a rectangular cross-section. The PTF between patches writes

$$Z_{re}^{d}=\rho_0 c\sum_i\frac{1}{N_i^d\sin\theta}\int_{S_r}\psi_i^d dS_r\int_{Se}\psi_i^d dS_e \tag{11}$$

where $\sin\theta=-j\sqrt{\frac{\left[(p\pi/L_x^d)^2+(r\pi/L_z^d)^2\right]}{(\omega/c)^2}-1}$, $N_i^d=\int_{S_d}(\varphi_i^d)^2dS_d$, φ_i^d is the i th rigid-walled acoustic mode shape of the duct,

$$\psi_i^d=\cos\left(\frac{p\pi}{L_x^d}x\right)\cos\left(\frac{r\pi}{L_z^d}z\right)\quad p,r=0,1,2..... \tag{12}$$

where L_x^d and L_y^d are the dimension of the duct.

The PTFs of MPPs are detailed hereafter. Considering a flexible micro-perforated panel, the pressure difference across the panel, p_1-p_2, generates the vibration of the air in the hole with a velocity u_h and that of the panel with a velocity u_p as shown in Fig. 3. Given the dimension of the hole is much smaller than the acoustic and flexural wavelengths of interests, the mean MPP vibration velocity can be approximated by [9]:

$$u_{MPP}=(1-\delta)u_p+\delta u_h \tag{13}$$

where δ is the perforation ratio.

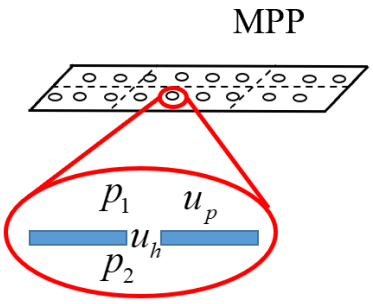

Figure 3. Pressure and velocity description over a MPP.

The viscous force in the hole along with the inertial force due to the air motion in the hole, contribute to the pressure difference across the MPP. Considering the vibration of the panel, the viscous force depends on the relative motion between the air in the hole and the structure, $u_h - u_p$. Therefore, one can write:

$$\Delta p = p_1 - p_2 = \mathrm{Re}\{Z_h\}(u_h - u_p) + j\,\mathrm{Im}\{Z_h\}u_h \tag{14}$$

where $\mathrm{Re}\{\}$ and $\mathrm{Im}\{\}$ denote the real and imaginary parts. Without flow, the acoustic impedance formulae established by Maa [23] are used to calculate the hole impedance Z_h, while in the presence of grazing flow, the formulae established in our previous work [25] are adopted.

The vibration velocity of the panel is expressed as:

$$u_s = Y_p f_p = Y_p \Delta p S_{patch}^{MPP}(1-\delta) \tag{15}$$

where Y_p is the mobility of the MPP plate; S_{patch}^{MPP} the surface area of the patch.

From Eqs. 13-15, the PTF between patches on the MPP, Y_{MPP}, can be written

according to Eq. 1 as,

$$Y_{MPP}=\frac{u_{MPP}}{\Delta p S_{patch}^{MPP}}=(1-\delta)[(1-\delta)+\delta\frac{\mathrm{Re}\{Z_h\}}{Z_h}]Y_p+\frac{\delta}{Z_h S_{patch}^{MPP}} \tag{16}$$

It can be seen that for a rigid MPP, $Y_p=0$, the PTFs of the MPP retreats to:

$$Y_{MPP}=\frac{\delta}{Z_h S_{patch}^{MPP}} \tag{17}$$

Current work deals with the MPPs under low acoustic excitation in the linear regime. Therefore, the vibration of MPP is ignored. Note that adding this effect, whenever necessary, poses no technical difficulty in the present modelling, since in this case, Eq. 16 can be employed.

If the side branch cavity is to be partitioned into smaller cavities, as shown in Fig. 2, the case can be regarded as a combination of multiple unit cells, each comprising a MPP facing and a backing sub-chamber. Assuming the unit cells are well separated from each other by solid partition walls, the side branch mobility Y^{MPP} and the impedance $Z^{SC_3SC_3}$ can be constructed by combing all the unit cells as a common subsystem as [21]:

$$Y^{MPP}=\begin{bmatrix} Y_1^{MPP} & & & & \\ & Y_2^{MPP} & & & \\ & & Y_i^{MPP} & & \\ & & & \ddots & \\ & & & & \ddots \end{bmatrix}$$

$$Z^{SC_3SC_3}=\begin{bmatrix} Z_1^{SC_3SC_3} & & & & \\ & Z_2^{SC_3SC_3} & & & \\ & & Z_i^{SC_3SC_3} & & \\ & & & \ddots & \\ & & & & \ddots \end{bmatrix}, \forall i \in [1,...,N_s] \quad (18)$$

where N_s is the number of sub-chambers in the side-branch cavity. For each unite cell, without considering the vibration of MPPs, the element of the corresponding mobility matrix Y_i^{MPP} and impedance matrix $Z_i^{SC_3SC_3}$ can be obtained by using Eqs. 17 and 9.

For the locally reacting case using honeycomb backing, the acoustic impedance of the cavity behind the MPP is $Z_{cavity}=-\cot(\omega D/c)$, where D is the depth of the backing cavity. In the present model, the MPP together with the backing partitioned cavity is characterized using the surface impedance: $Z_{panel}=Z_{MPP}+Z_{cavity}$. The PTF calculation of the backing cavity is thus not needed. Consequently, the matrix Z in Eq. 8 retreats to

$$Z=\begin{bmatrix} Z^{MC_1MC_1}-Z^{d1d1} & Z^{MC_1MC_2} & Z^{MC_1MC_3} \\ Z^{MC_2MC_1} & Z^{MC_2MC_1}-Z^{d2d2} & Z^{MC_2MC_3} \\ Y^{MPP}S_eZ^{MC_3MC_1} & Y^{MPP}S_eZ^{MC_3MC_2} & Y^{MPP}S_eZ^{MC_3MC_3}-I \end{bmatrix}$$ and Eq. 17 becomes

$$Y_{MPP}=\frac{1}{Z_{panel}S_{patch}^{MPP}}.$$

Once Eq. 8 is resolved, the patch response can be obtained, which allows the

calculation of all other acoustic quantities such as Transmission Loss (TL), sound absorption coefficient and reflection coefficient. More specifically, TL is defined as:

$$TL=10\log_{10}\frac{\prod_{in}}{\prod_{out}} \tag{19}$$

where

$$\prod_{in}=\frac{|p_i|^2}{2\rho_0 c}S_1 \tag{20}$$

$$\prod_{out}=\frac{1}{2}\int_{S_2}\mathrm{Re}\left\{P_2V_2^*\right\}dS_2 \tag{21}$$

are the incident and transmitted sound power, respectively. $|p_i|$ is the acoustic pressure amplitude of the incidence wave; V_2 and P_2 are the normal velocity and the sound pressure at interface *C2*; S_1 and S_2 are the total surface area of *C1* and *C2* and the superscript * represents the complex conjugate.

The sound reflection coefficient, R, is defined as the ratio between the reflected sound power at *C1*, $\prod_r$, and the incidence sound power, $\prod_{in}$, which writes,

$$R=\frac{\prod_r}{\prod_{in}}=\frac{\prod_{in}-\prod_t^1}{\prod_{in}} \tag{22}$$

where $\prod_t^1$ is the transmitted sound power through *C1*, calculated by

$$\prod_t^1=\frac{1}{2}\int_{S_1}\mathrm{Re}\left\{P_1V_1^*\right\}dS_1 \tag{23}$$

in which V_1 and P_1 are the normal velocity and the sound pressure at *C1*, respectively. The sound absorption coefficient α describing the fraction of the sound power absorbed by the MPP absorber when an incidence plane wave propagates through the duct can then be obtained as,

$$\alpha = \frac{\prod_t^1 - \prod_{out}}{\prod_{in}} \tag{24}$$

3. Experimental validations

Experiments were first conducted to validate the PTF model and the implemented calculation scheme. The TL was measured by using the standard four-microphone-two-source method [30]. The sound absorption coefficient α can then be deduced by

$$\alpha = \frac{\prod_{in}^{\exp} - \prod_{out}^{\exp} - \prod_r^{\exp}}{\prod_{in}^{\exp}} \tag{25}$$

where

$$\prod_{in}^{\exp} = \frac{\left|p_i^{\exp}\right|^2}{2\rho_0 c_0} S_{duct} \tag{26}$$

$$\prod_r^{\exp} = \frac{\left|p_r^{\exp}\right|^2}{2\rho_0 c_0} S_{duct} \tag{27}$$

are the measured incident and reflected sound power in the inlet duct, respectively. In Eqs. 26 and 27, S_{duct} is the cross-section area of the duct; $\left|p_i^{\exp}\right|$ and $\left|p_r^{\exp}\right|$ are the measured pressure amplitude of the incident and reflected waves in the inlet part of the duct, which can be obtained from the two upstream microphones (M1 and M2 in Fig. 4) by using model-decomposition method. $\prod_{out}^{\exp}$ is the measured transmitted sound power, which can be derived according to the definition of the TL as

$$\prod_{out}^{\exp} = \frac{\prod_{in}^{\exp}}{10^{TL/10}} \tag{28}$$

The experimental setup is sketched in Fig. 4. The cross section of the duct is 100 x 100 mm with a cut-on frequency of 1700 Hz. Four 1/4-inch microphones were used with two of them flush-mounted upstream the silencer and two others downstream. The separation distance between the microphones is shown in Fig. 4.

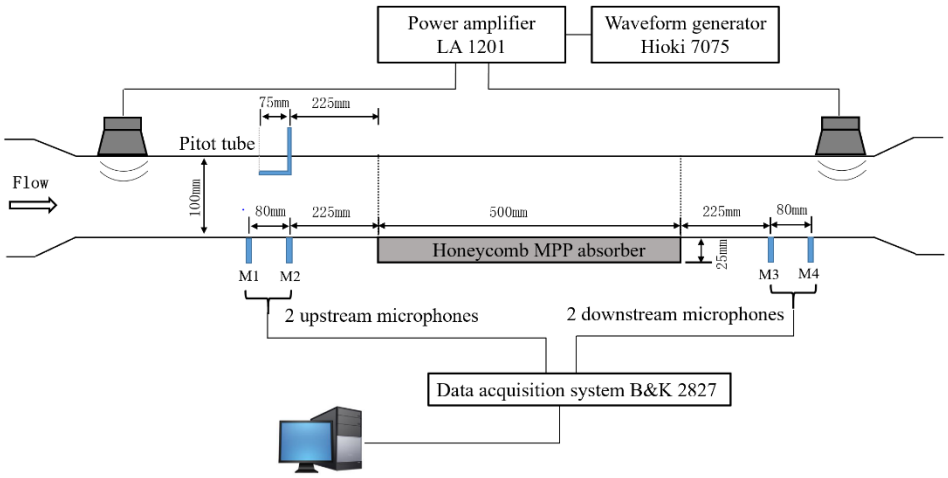

Figure 4. Experimental setup.

The test sample, shown in Fig. 5, is a single layer aluminum MPP backed by a honeycomb structure with a thickness of 25 mm, forming a honeycomb MPP liner. With the honeycomb structure, the acoustic waves travel predominantly along the depth direction within the cavity, i.e. perpendicular to the MPP, so that the MPP exhibits locally reacting behavior. The MPP is 100mm wide and 500mm long, with a perforation ratio of 0.945%. The diameter of the perforated hole and the thickness of the MPP are both 0.5mm.

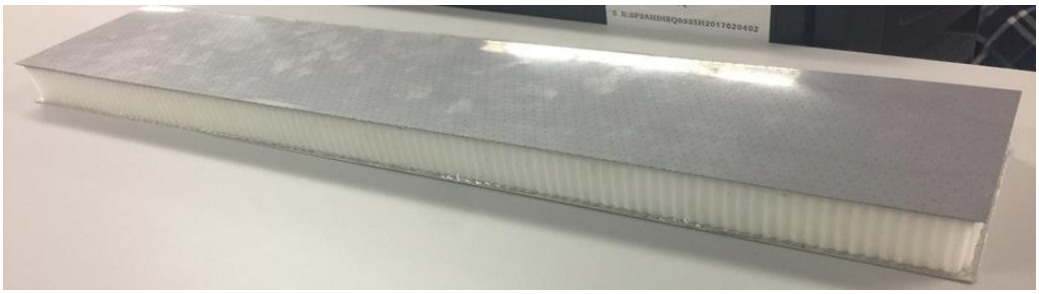

Figure 5. Test sample.

The accuracy of the PTF calculation is validated through comparisons with the measured data. The TL and the sound absorption coefficient, α, of the honeycomb MPP liner ($d = t = 0.5mm$ and δ=0.954%) at three different grazing flow velocities are presented and compared in Figs. 6-8. The comparison shows that the prediction results fit the experimental data reasonably well for various tested flow speeds in terms of TL, α, bandwidth as well as the location of their peak frequencies. The observed deviations of the predicted maximum values from the measured ones are mainly due to the venerable signal to noise ratio (SNR) obtained during experiments. In fact, the presence of the flow generated considerable background noise. As the level of the imposed acoustic excitation should be limited within the linear regime of the MPP, the SNR could not be further increased. Therefore, the predicted high TL around the peak location could not be measured during experiments. Nevertheless, the above validations confirm the validity of the PTF approach.

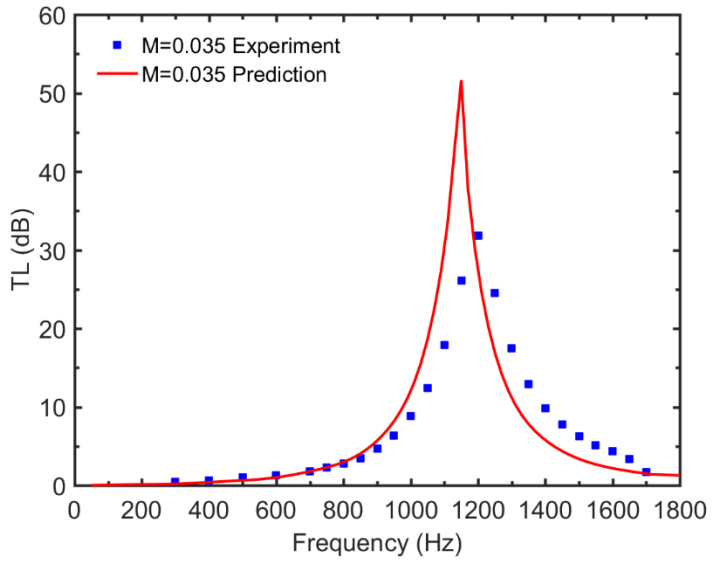

(a)

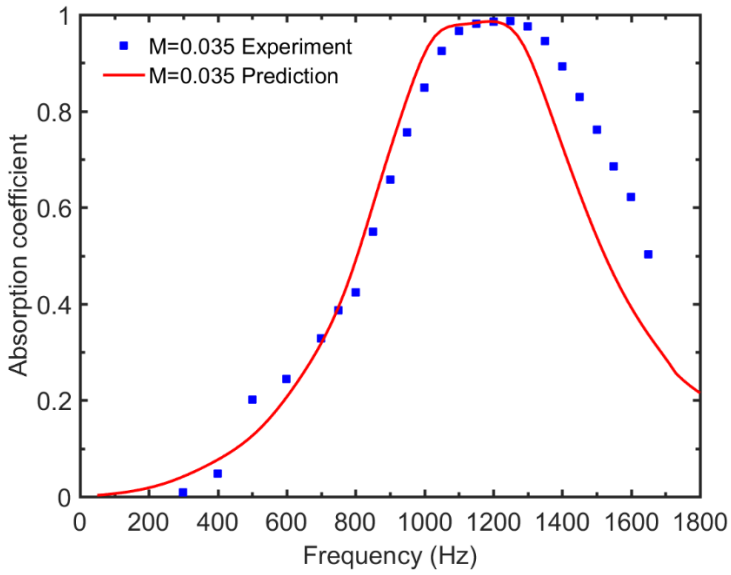

(b)

Figure 6. Comparisons between predicted and experimental results at $M = 0.035$. (a) TL; (b) sound absorption coefficient.

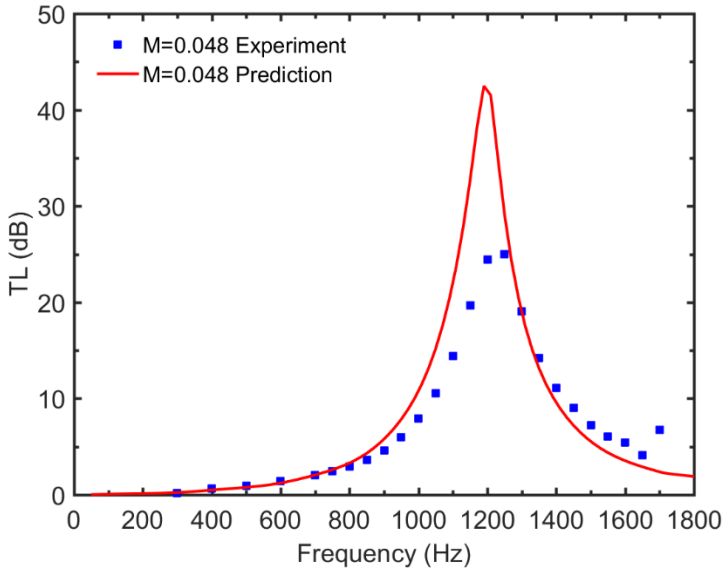

(a)

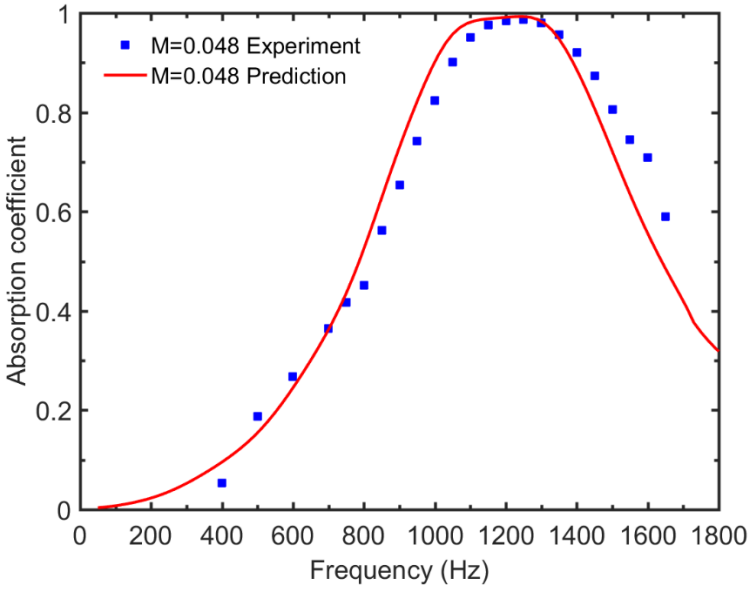

(b)

Figure 7. Comparisons between predicted and experimental results at $M = 0.048$. (a) TL; (b) sound absorption coefficient.

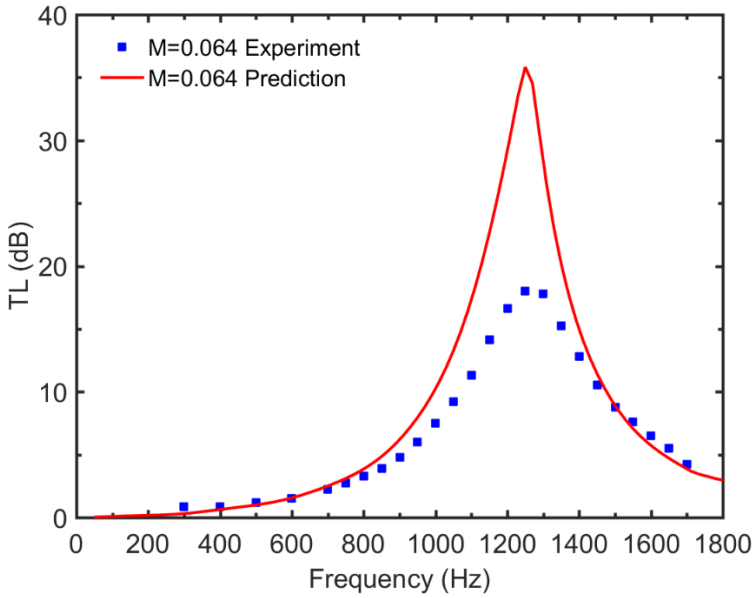

(a)

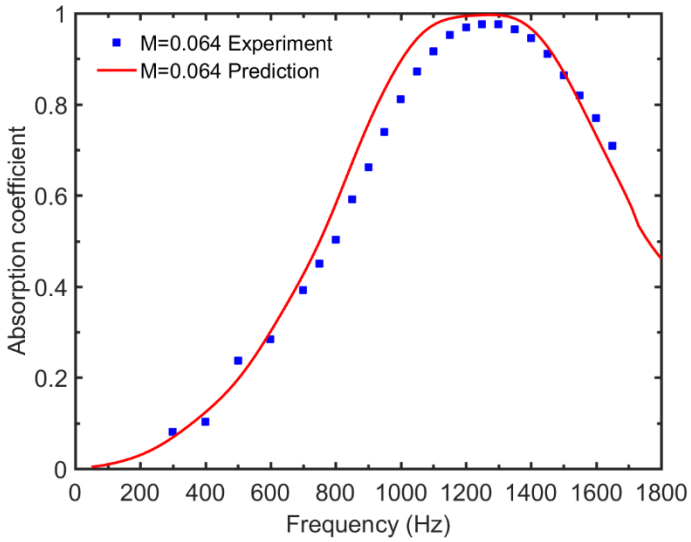

(b)

Figure 8. Comparisons between predicted and experimental results at $M = 0.064$. (a) TL; (b) sound absorption coefficient.

4. Numerical results and analyses

To gain understanding on the sound attenuation mechanism of the MPP silencers and provide guidelines for their design in flow ducts, influences of the flow velocities, solid partition arrangements in the backing cavity, perforation ratios, hole diameters and panel dimensions are investigated. By employing the validated PTF approach, the effects of these parameters on the acoustic attenuation performance of MPP liner as well as on its optimal design are scrutinized. In the analyses, the hole diameter and the panel thickness of MPPs are taken to be the same. The dimension of the investigated system (Fig. 1) is the same as the one used in experiment, described in Fig. 4.

4.1 Grazing flow effects

TL curves of a non-partitioned MPP silencer ($d = t = 0.5mm$ and δ=0.954%) under different flow velocities are compared in Fig. 9. A typical TL curve at $M = 0.05$ is first taken for analyses. Several dips and peaks appear in the TL curves, resulting in relatively low but broadband acoustic attenuation. The peaks are due to the coupling of the MPP with both the backing cavity and the main duct, with their locations corresponding to the coupled system natural frequencies. With grazing acoustic wave incidence, the streamwise or grazing modes of the backing cavity (along duct length direction) are activated to generate these dips [31]. These streamwise modes occur at frequencies corresponding to $f_{A,n}$=$nc/2L$, with L being the length of the backing cavity (500 mm in the present configuration) and n corresponding to the number of

half-wavelength, both in the duct length direction. The sound pressure distribution at one selected dip on the TL curve, at $M=0.05$ and $f = f_{A,4} = 1377Hz$, around one streamwise mode of the backing cavity, is presented in Fig. 10. It can be seen that the sound pressure distribution features four nodal planes in the backing cavity, corresponding to four half-wavelengths. Meanwhile, the streamwise locations of these nodal planes in the backing cavity are coincident with those in the main duct. Consequently, the pressure across the MPP is almost the same and in-phase, thus resulting small pressure difference across the MPP. Under this circumstance, the vibration velocity of the air inside the hole of the MPP is trivial and eventually neutralized as expected, thus annulling possible energy dissipation.

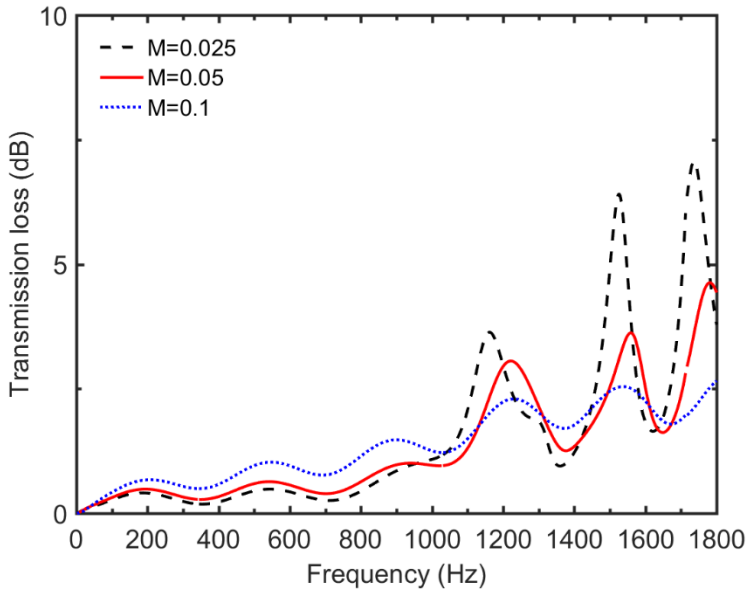

(a)

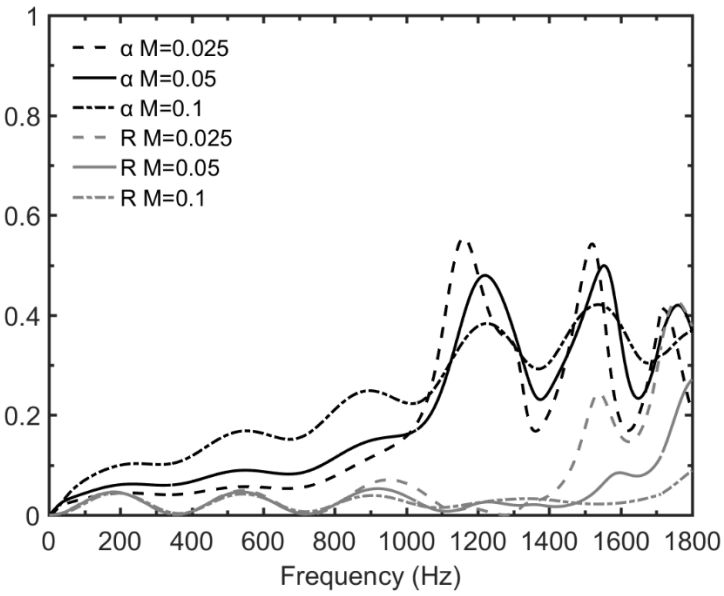

(b)

Figure 9. Silencing performance of a MPP silencer ($d = t = 0.5mm$ and δ=0.954%) without partitions under different flow velocities. (a)TL; (b) sound absorption and reflection coefficient.

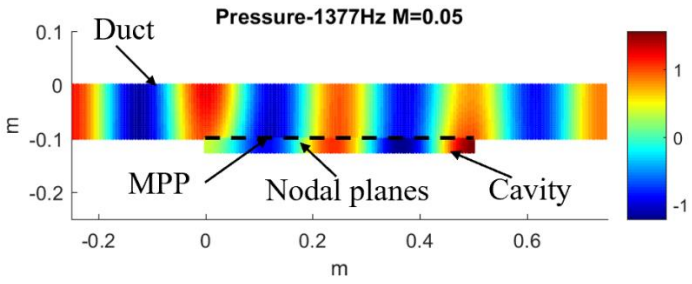

Figure 10. Sound pressure distribution (Pa) with a MPP liner without partitions at $f = 1377$ Hz and $M = 0.05$.

Comparison in Fig. 9a also indicate that higher speed flow slightly enhances the

sound attenuation in the low frequency range, but lifts up the troughs, smooths out and reduces the peaks while shifting them to higher frequencies roughly above 1000 Hz, and finally results in a more flattened TL curve when flow speed increases. Note the locations of the troughs are not affected by the grazing flow, consistent with the analyses above in that streamwise resonance frequencies of the backing cavity only depend on its length. As the peaks are induced by the coupling in the duct system, and the grazing flow alters the impedance of the MPP and thus the coupling effects, variations in the peak values and peak locations are thus observed.

To better understand the underlying physical phenomena, corresponding sound absorption (α) and reflection (R) coefficient curves are plotted in Fig. 9b. It can be seen that both dissipation and reflection contribute to the observed overall sound attenuation, thus exhibiting a hybrid behavior, though the former seems to be more dominant. The overall effects of the grazing flow on α are in line with the variations of the corresponding TL curve.

By adding partitions inside the backing cavity, a honeycomb or locally reacting MPP silencer is formed, with corresponding TL and α curves presented in Fig. 11. Figure 11a shows that, different from the non-partitioned case with several dips and peaks, the TLs of the honeycomb MPP silencers exhibit only one major peak, typical of one single degree of freedom behavior as a result of the partition. Obviously, the peak is induced by the depth-wise quarter resonance in the backing cavity.

To further quantify the phenomena, the variations of the maximum TL value, $TL_{\max}$, peak frequency, f_p, and 5dB TL bandwidth, $W = \left| f_u^{TL} - f_l^{TL} \right|$, are used to describe the grazing flow effects on the TL, where f_u^{TL} and f_l^{TL} are the lower and upper frequencies corresponding to 5 dB TL. Fig. 11a shows the variation of these defined parameters for three selected flow speeds. It can be seen that the grazing flow shifts the location of the peak frequency f_p to a higher frequency when flow speed increases, reduces the peak value $TL_{\max}$ and broadens the bandwidth W. Figure 11b shows that the grazing flow affects the corresponding sound absorption coefficient in a similar way as TL in terms of the peak frequency shifting, peak value variation and bandwidth enlargement. It is worth noting that the presence of the grazing flow typically results in a wider acoustic attenuation bandwidth. Consequently, although the grazing flow can reduce the peak value, compared to the no-flow condition, better broadband acoustic attenuation performance could be expected provided that the MPP parameters are properly selected.

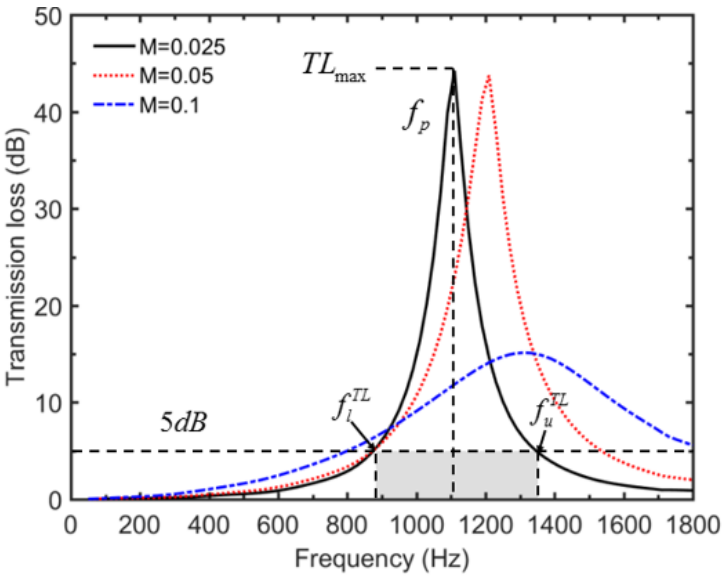

(a)

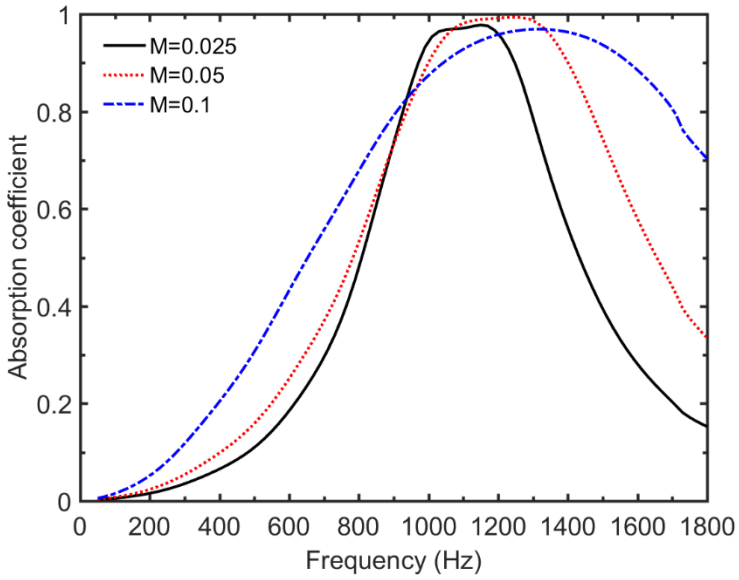

(b)

Figure 11. Silencing performance of a honeycomb MPP silencer ($d = t = 0.5mm$ and δ=0.954%) under different flow velocities. (a) TL; (b) sound absorption coefficient.

4.2 Effects of the partition inside the backing cavity

The TL, the absorption and the reflection coefficient curves of the MPP silencers ($d = t = 0.5mm$ and δ=0.954%) with a backing cavity having different solid partitions at $M = 0.05$ are compared in Fig. 12. The results indicate that different partitions significantly affect the acoustic attenuation performance of the MPP silencers. Generally speaking, increasing the number of partitions reduces the number of ripples on both the TL curves and the absorption curves, giving rise to a narrower bandwidth but a higher peak value. Meanwhile, the reflection effect also decreases with the partitions and finally becomes negligible compared to the absorption effect. Further increasing the partitions push the curves gradually approaching the locally reacting (honeycomb) case with only one dominant peak. This suggests that, to achieve the locally reacting effect, it is not necessary to use a honeycomb structure which is usually designed to pair up one hole in the panel with one cell in the backing cavity or a densely partitioned design. As long as the size of the partitioned sub-cavity is sufficient small as compared to the acoustic wavelength, wave motion in the sub-cavity is basically confined to the depth direction so that the surface impedance can be considered as locally reacting.

The increase in the absorption (Fig.12b) and the reduction in the reflection (Fig.12c) with increasing number of partitions indicate a transition in the acoustic attenuation mechanism from a hybrid one (both dissipation and reflection) to almost a purely dissipative one. Therefore, most of the attenuated acoustic energy are dissipated

by MPP silencers with sufficient partitions or honeycomb MPP silencers.

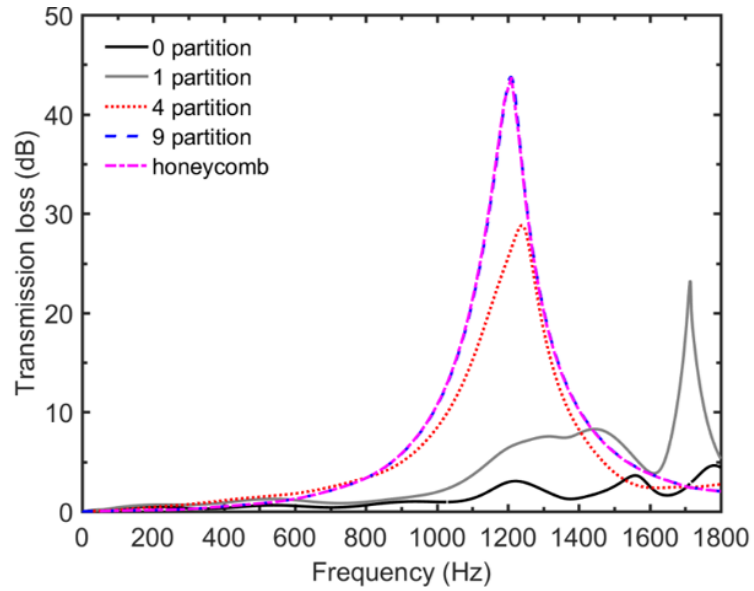

(a)

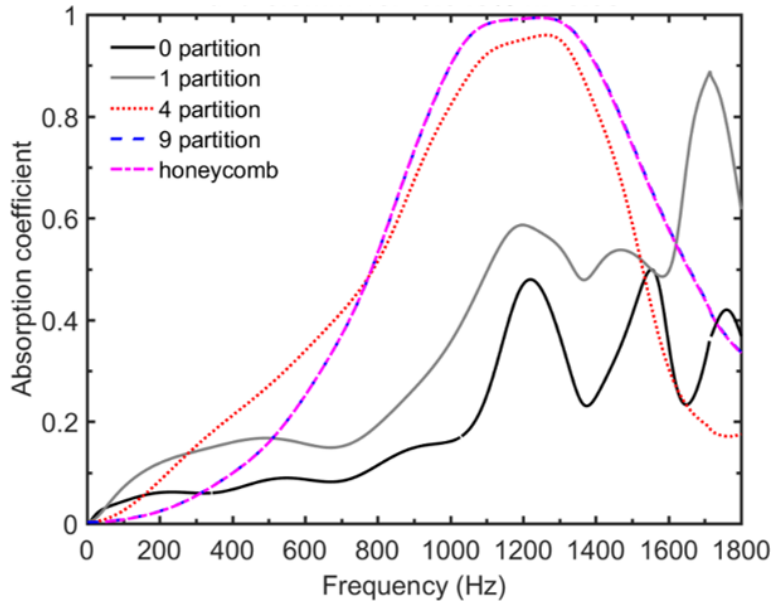

(b)

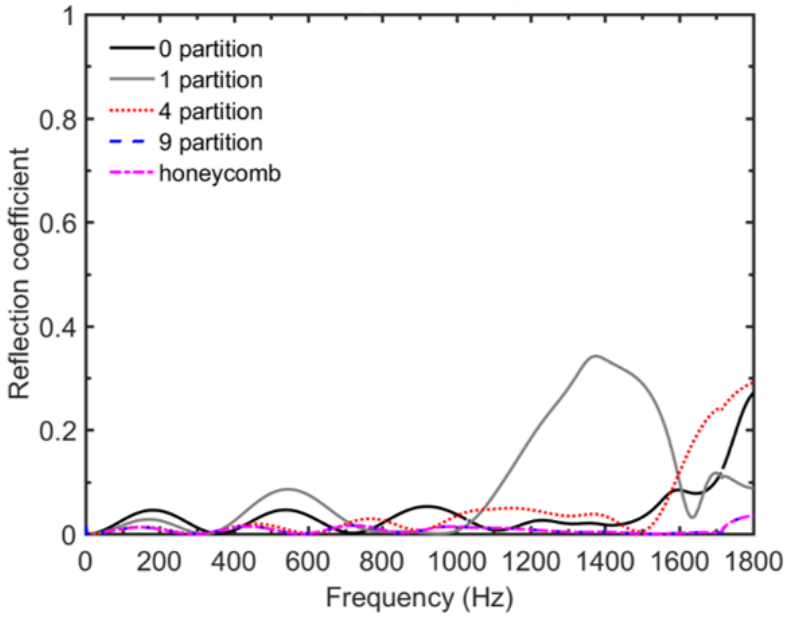

(c)

Figure 12. Silencing performance of MPP silencers ($d = t = 0.5mm$ and δ=0.954%) with different partitions at $M = 0.05$. (a) TL; (b) sound absorption coefficient; (c) reflection coefficient.

4.3 Effects of panel parameters

4.3.1 Hole diameter

The maximum TL value $TL_{\max}$, peak frequency f_p and 5dB TL bandwidth W of honeycomb MPP absorbers with different hole diameters but the same perforation ratios (1%) with and without grazing flow are shown in Fig. 13. In the absence of the flow, it can be seen that increasing the diameter of the hole reduces the peak frequency. Meanwhile, the maximum TL value increases first and then decreases, while the TL bandwidth reduces. In the presence of grazing flow, the same trend can be observed.

Therefore, it can be expected that, to achieve a broadband acoustic attenuation for locally reacting case, the panels with small holes are preferred, irrespective of whether flow exists or not. This is understandable since for locally reacting silencer, the sound energy attenuation is predominantly due to the dissipation effects and smaller holes can usually provide a wider absorption bandwidth. Therefore, to achieve a broadband noise control, a locally reacting silencer with small holes is usually a better choice. This is different from the non-locally reacting case relying on hybrid sound attenuation investigated in Ref. [21], in which case, to achieve optimal broadband silencing performance, a balance between the dissipation and reflection effects needs to be struck. This also explains the reason why, for non-partitioned silencers shown in Fig. 14, the panel with smallest hole size $d = t = 0.2mm$ cannot provide the best acoustic attenuation performance.

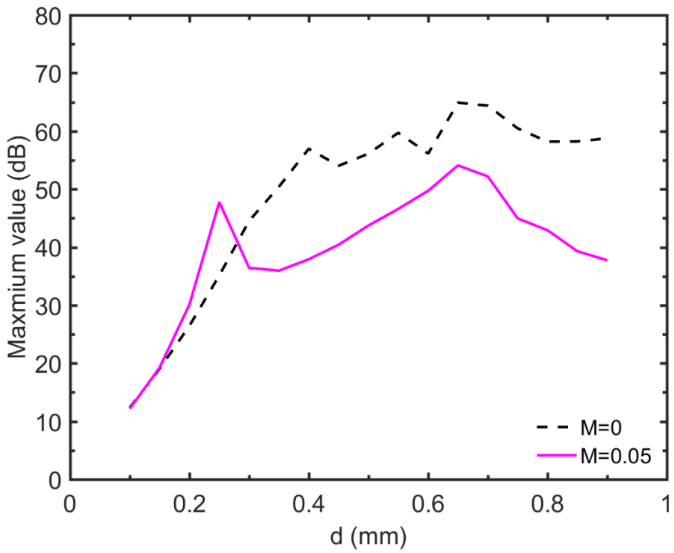

(a)

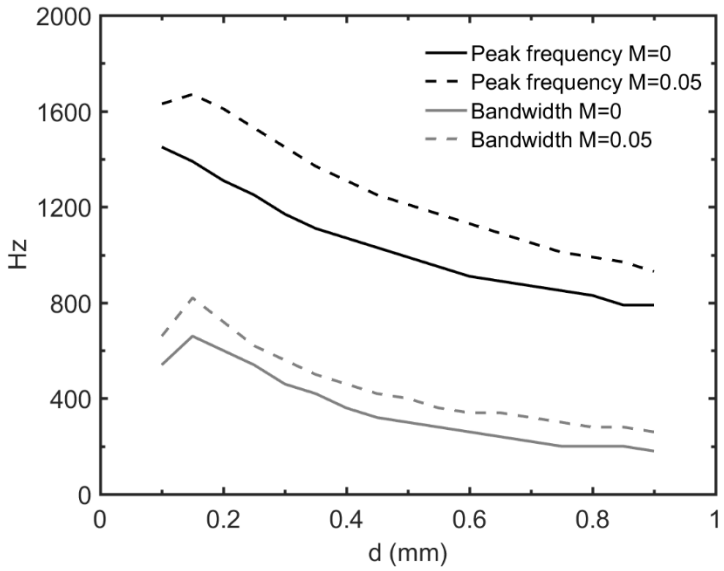

(b)

Figure 13. (a) TL peak value; (b) TL peak frequency and bandwidth of MPP silencers with different hole diameters.

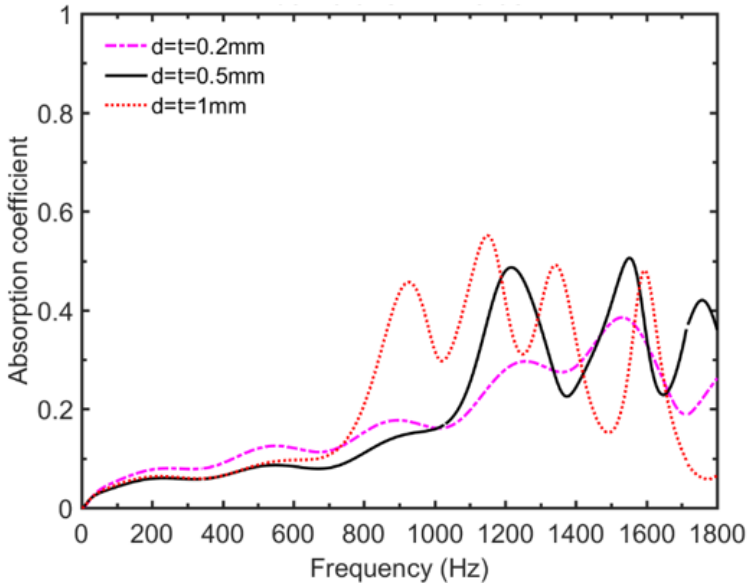

Figure 14. TLs of non-partitioned MPP silencers with different hole diameters at $M = 0.05$.

4.3.2 Perforation ratio

The effects of the perforation ratio on the honeycomb MPP silencers with and without grazing flow are shown in Fig. 15. It can be seen that, without flow, when the perforation ratio increases, TL peak frequency is shifted to a higher frequency, whilst the peak TL value first increases and then decreases. However, the TL bandwidth keeps almost constant, seemingly unaffected by the perforation ratio. In the presence of grazing flow, the effects of panel perforation ratio on honeycomb MPP silencers are similar to the no-flow condition.

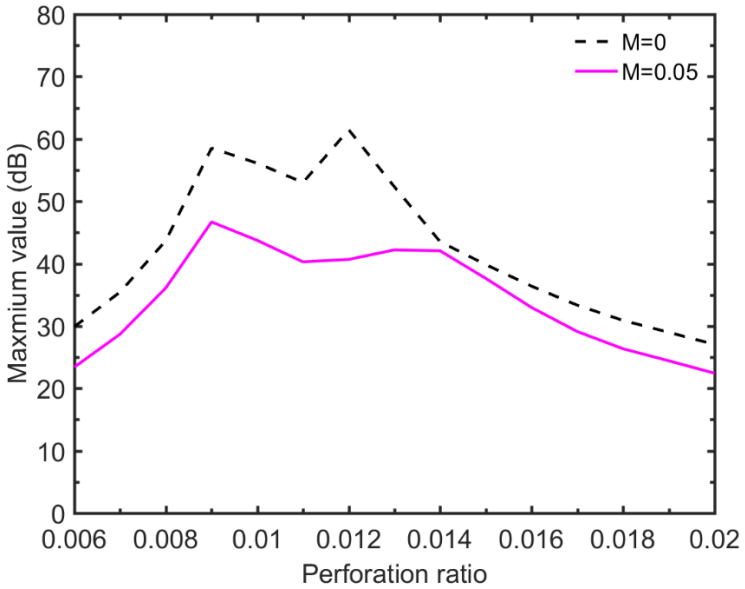

(a)

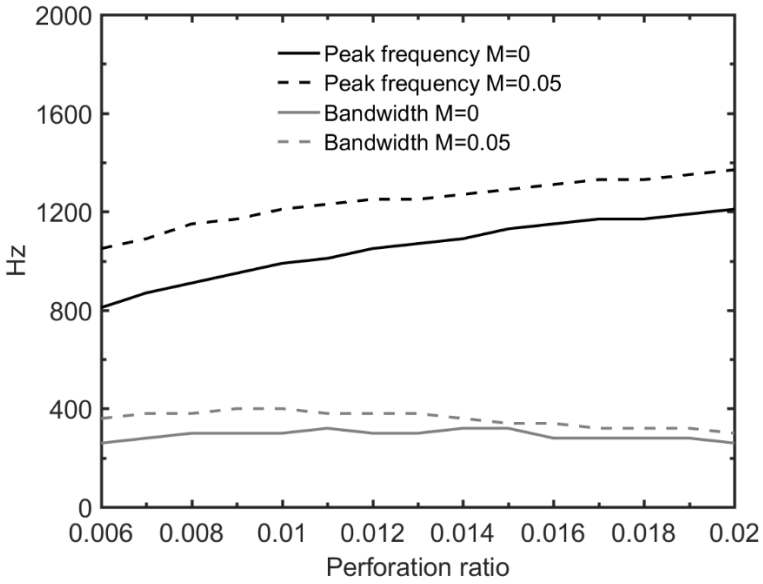

(b)

Figure 15. (a) TL peak value; (b) TL peak frequency and bandwidth of MPP silencers with different perforation ratios.

4.3.3 Panel dimension

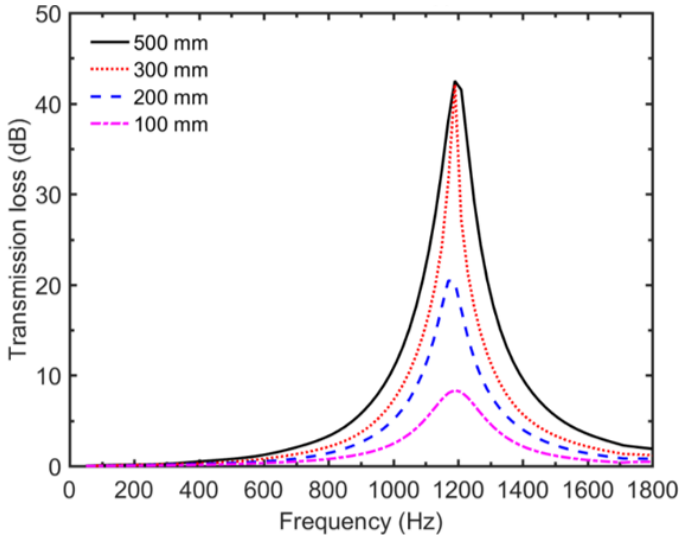

(a)

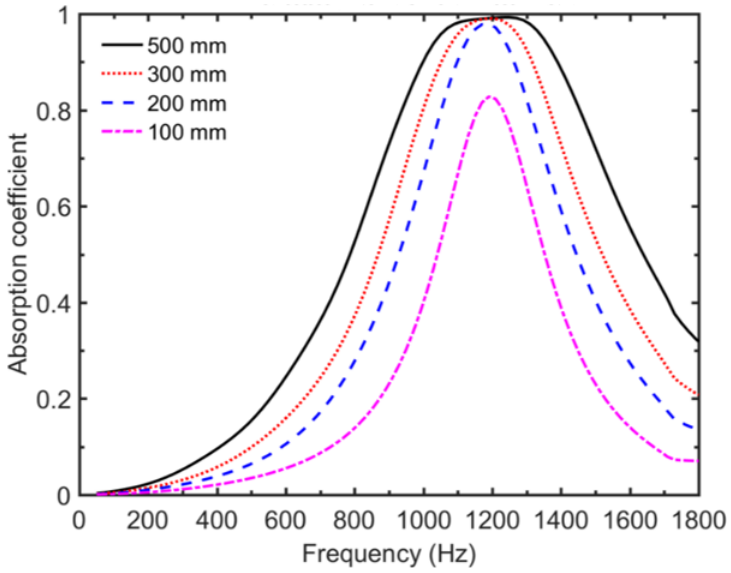

(b)

Figure 16. Silencing performance of honeycomb MPP silencers ($d = t = 0.5mm$ and δ=0.954%) with different panel lengths at $M = 0.05$. (a) TL; (b) sound absorption coefficient.

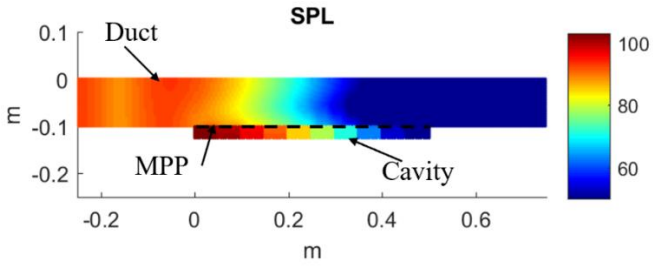

Figure 17. Sound pressure field (dB) with a MPP liner with a backing cavity containing nine partitions at the peak frequency $f = 1190$ Hz and $M = 0.05$.

The effect of the MPP panel dimension on the acoustic performance of MPP liners is investigated. To this end, honeycomb MPP silencers with different panel lengths are

compared in terms of TL, as shown in Fig. 16. It is clear that the TLs of the locally reacting MPP silencers depend significantly on the size of the panel. More specifically, the maximum level and the bandwidth of both the TL and the absorption coefficient curves all increase with the panel length, without, however, noticeable variations in the peak location. The pressure field of a MPP silencer with a backing cavity containing nine partitions at the peak frequency $f = 1190Hz$ and $M = 0.05$ is shown in Fig. 17. It can be seen that the energy intensity of the acoustic wave, propagating in the duct, decays continuously in the downstream direction so that more acoustic energy can be dissipated when the panel becomes longer. Therefore, a sufficiently large panel is needed when designing locally reacting MPP silencers for effective noise attenuation.

The same issue is revisited for non-partitioned MPP silencers, as shown in Fig. 18 at $M = 0.05$. As the length of the panel can change the coupling of the entire system, in particular the frequencies at which the streamwise modes of the backing cavity appear, it is obvious that the number of dips and peaks on the TL curves as well as their locations are all affected by the dimension change of the panel. The variation trend, however, is much more complex than the case of locally reacting silencers. Consequently, unlike the case of locally reacting silencer, which always requires the use of the largest possible dimension, the optimal length of a non-partitioned silencer needs to be tuned to cope with a targeted frequency bandwidth.

To better understand the way to select the optimal value of the panel length for

non-partitioned silencers, the pressure field of a non-partitioned MPP silencer with a panel length of 500 mm at one peak frequency $f = 1221Hz$ and $M = 0.05$ is plotted in Fig. 19. It can be observed that, the energy distribution of the acoustic wave, propagating in the duct, does not necessarily decay continuously in the streamwise direction in the lined part, which is different from the locally reacting case. The complex sound pressure distribution across the MPP panel also testifies the increasing complexity of the acoustic coupling in the non-partitioned silencer. In such cases, a system optimization, with the help of the PTF model developed in the current work, becomes possible and necessary.

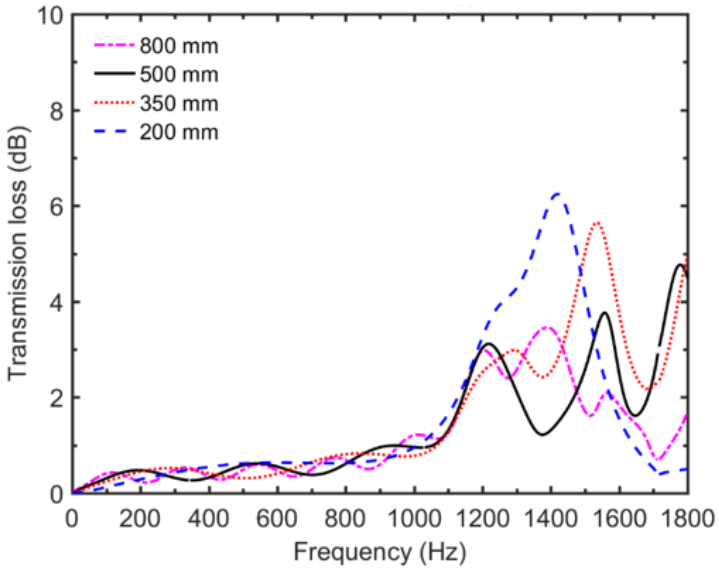

Figure 18. TLs of non-partitioned MPP silencers ($d = t = 0.5mm$ and δ=0.954%) with different panel lengths at M =0.05 .

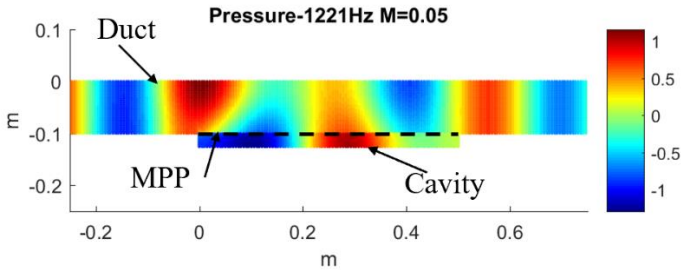

Figure 19. Sound pressure distribution (Pa) with a non-partitioned MPP liner ($d = t = 0.5mm$ and δ=0.954%) with a panel length of 500mm at one peak frequency $f = 1221Hz$ and $M = 0.05$.

4.4 Optimizations of MPPs in flow ducts

The above discussions indicate that TLs of MPP silencers are sensitive to the system parameters. Therefore, a systematic system optimization is needed to target a prescribed frequency range for effective sound attenuation. As an illustrative example, optimizations are performed through the tuning of two MPP parameters: the perforation ratio δ and the diameter of the hole d. For a given incident sound power, the total transmitted sound power in a prescribed frequency range is used to evaluate the silencing performance of the system, which is expressed as

$$\Pi_{sum}^{out}(\mathrm{d},\delta)=\int_{f_l}^{f_u}\prod^{out}(f)df=\sum_{i=1}^{N_f}\Pi_i^{out} \tag{29}$$

where f_l and f_u are the lower and upper bounds of the target frequency range,

respectively; N_f is the number of discrete frequency points used for the calculation and Π_i^{out} is the transmitted sound power at one discrete frequency point i in the target frequency range. The optimization process is defined to find the optimal parameters, d and δ, to warrant a minimum total transmitted sound power in the target frequency range. The problem can be formulated as:

$$\text{min. } \Pi_{sum}^{out}(d,\delta) \tag{30a}$$

$$\text{s.t. } 0.1 \le d \le 0.9,\ \Delta d = 0.05mm \tag{30b}$$

$$0.6\% \le \delta \le 2\%,\ \Delta\delta = 0.1\% \tag{30c}$$

where Π_{sum}^{out} is the objective function; min. is the abbreviation of *minimize* and s.t. is the abbreviation of *subject to*. The constraint condition Eq. 30b imposes a restriction on d, which is incremented by a step of 0.05 mm (17 points in total). δ is varied within the constraint range from 0.6% to 2% with an increment of 0.1% amounting to a total of 15 points (Eq. 30c). Overall, this results in 255 different combinations of d and δ.

The first example considers a broadband optimization, targeting a frequency range from 200 to 1700 Hz with an increment of 10 Hz. Owing to the sub-structural treatment of the PTF approach, only the subsystems undergoing changes during the optimization process need to be recalculated in each optimization loop. In the present case, it is the mobility matrix of the MPP Y^{MPP} in Eq. 8, while the uncoupled acoustic quantities of

other subsystems remain unchanged. Finally, the computational time for the calculations of these 255 cases is less than 10 minutes using a standard personal computer, which further demonstrates the efficiency of the PTF approach for the design of MPPs in complex acoustic environment.

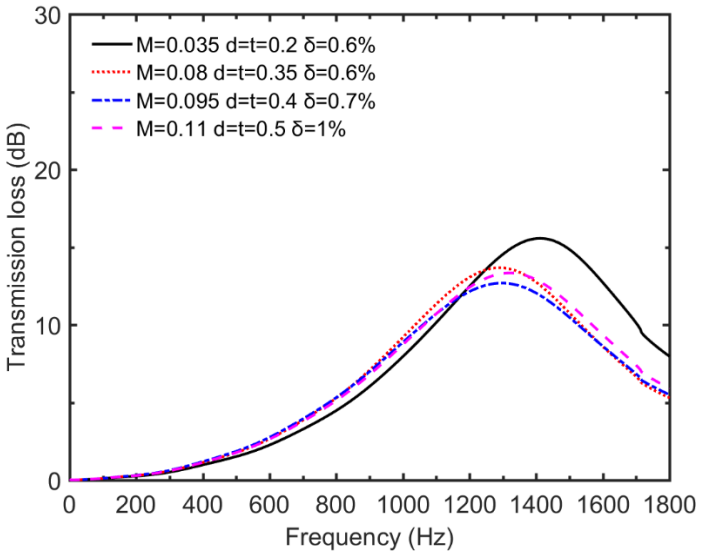

Figure 20. Optimized TL curves of locally reacting MPP silencers (9 partitions) under different flow velocities.

The effects of the grazing flow at four different flow speeds on the optimized results for locally reacting MPP silencers (with nine partitions) are shown in Fig. 20. As is seen in the figure, the optimized hole size and perforation ratio tend to increase with respect to flow velocity. Consequently, a larger hole with a higher perforation ratio would be preferable in a locally reacting silencer to cope with a duct with a higher speed flow. As the analyses in Section 4.1 indicate that the presence of the grazing flow shifts the TL peak to a higher frequency when flow speed increases, the diameter of the hole

needs to be increased accordingly to downshift the TL peak within the target bandwidth. This may explain why the optimized values of the hole diameter increase with the flow velocity. As the presence of the grazing flow typically leads to a wider acoustic attenuation bandwidth as well, it is also relevant to note that it is possible to use panels with a larger hole size to achieve broadband silencing performance under high flow velocity while making sure that the overall acoustic performance is not significantly deteriorated compared to low flow velocity condition as shown in Fig. 20.

The above observation has been verified to also hold for non-locally reacting MPP silencers with a non-partitioned backing cavity (results not shown here). In summary, the presence of grazing flow generally benefits the achievement of broadband acoustic attenuation performance by using panels with larger hole size, irrespective whether the MPP silencer is locally reacting or not.

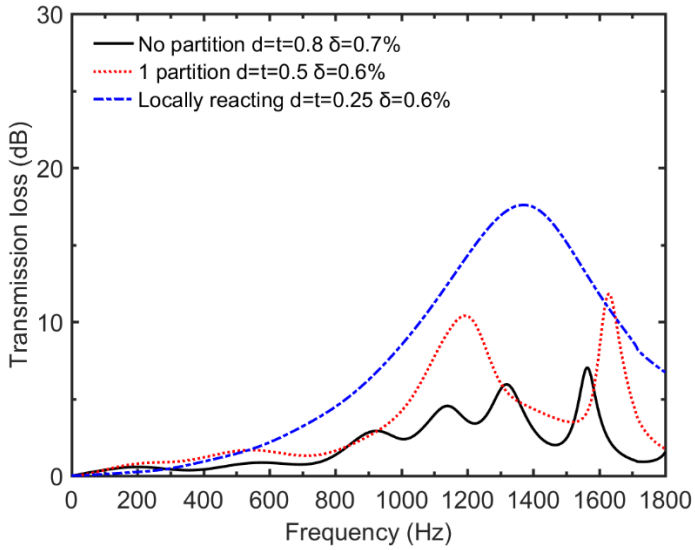

Figure 21. Optimized TL curves of MPP silencers with backing cavity having different partitions at $M = 0.05$.

Optimized TL curves of MPP silencers having different partitions inside the backing cavity are presented in Fig. 21. The optimization process finally results in optimal combinations with $d = 0.8mm$ and δ=0.7% , $d = 0.5mm$ and δ=0.6% , and $d = 0.25mm$ and δ=0.6% for MPP silencers with zero, one and nine partitions (locally reacting), respectively. It can be seen that the optimized value of the hole size decreases with the number of partitions in the backing cavity. Since the dissipation effect increases and the reflection effect decreases with respect to the number of partitions (Fig. 12) and smaller hole size can provide enhanced dissipation effect and weakened reflection effect, the optimization process leads to a smaller hole size when the number of partitions increases. Meanwhile, it can also be seen that the optimized silencing performance of the MPP liners gradually increases when the number of partitions increases. However, this is at the expense of increasing the difficulty in manufacturing smaller holes on the MPP panel.

5. Conclusions

The acoustic behavior of micro-perforated panel liners in flow ducts are numerically investigated using a revamped PTF model after experimental validations. The effects of solid partitions inside the backing cavity, as well as those of the grazing flow, the hole diameter, the perforation ratio and the panel dimension are systematically investigated to provide guidance for MPP silencer design. The following conclusions

can be drawn from the numerical analyses.

Grazing flow typically shifts the TL peaks to a higher frequency, alters its maximum level and flattens the TL curve with a wider bandwidth. The effects of the hole diameter and the perforation ratio of a MPP liner on its silencing performance under grazing flow are basically similar to cases without flow. However, the increasing flow speed generally requires the use of MPPs with a larger hole size to ensure broadband acoustic attenuation.

Partitions inside the backing cavity of a MPP liner significantly impact on its acoustic attenuation performance. Generally speaking, a sufficient number of partitions would be enough to warrant locally-reacting effects in a partitioned MPP liner, which is conducive to more effective broadband noise control.

The MPP dimension affects the acoustic performance in both locally and non-locally reacting cases. In the former, a large enough panel is needed to ensure an effective sound attenuation. The latter, however, exhibits a less intuitive influencing manner, since the size of the MPP needs to be meticulously determined in order to create the desired system coupling and effective sound attenuation within a prescribed frequency range. This can be materialized through a systematic system optimization. In that sense, the model established in the current work would serve as a useful and indispensable tool.

Acknowledgements

The authors thank the support from Research Grant Council of the Hong Kong SAR (PolyU 152036/18E)

References:

[1] H. Fuchs and X. Zha, "Acrylic-glass sound absorbers in the plenum of the Deutscher Bundestag," *Applied Acoustics,* vol. 51, no. 2, pp. 211-217, 1997.

[2] J. Kang and H. V. Fuchs, "Predicting the absorption of open wave textiles and micro-perforated membranes backed by an air space," *Journal of Sound & Vibration,* vol. 220, no. 5, pp. 905-920, 1999.

[3] J. Kang and M. Brocklesby, "Feasibility of applying micro-perforated absorbers in acoustic window systems," *Applied Acoustics,* vol. 66, no. 6, pp. 669-689, 2005.

[4] K. Hoshi, T. Hanyu, T. Okuzono, K. Sakagami, M. Yairi, S. Harada, S. Takahashi and Y. Ueda, "Implementation experiment of a honeycomb-backed MPP sound absorber in a meeting room," *Applied Acoustics,* vol. 157, p. 107000, 2020.

[5] X. Yu, F. Cui, and L. Cheng, "On the acoustic analysis and optimization of ducted ventilation systems using a sub-structuring approach," *The Journal of the Acoustical Society of America,* vol. 139, no. 1, pp. 279-289, 2016.

[6] Y. Wuzhou, "Design and noise reduction of elevated road barrier of micro-perforated panels with linear-change cavity," *Environmental Pollution & Control,* vol. 7, pp. 67-69, 2008.

[7] F. Asdrubali and G. Pispola, "Properties of transparent sound-absorbing panels for use in noise barriers," *The Journal of the Acoustical Society of America,* vol. 121, no. 1, pp. 214-221, 2007.

[8] G. Li and C. K. Mechefske, "A comprehensive experimental study of micro-perforated panel acoustic absorbers in MRI scanners," *Magnetic Resonance Materials in Physics, Biology and Medicine,* vol. 23, no. 3, pp. 177-185, 2010.

[9] L. Maxit, C. Yang, L. Cheng, and J.-L. Guyader, "Modeling of micro-perforated panels in a complex vibro-acoustic environment using patch transfer function approach," *The Journal of the Acoustical Society of America,* vol. 131, no. 3, pp. 2118-2130, 2012.

[10] C. Yang and L. Cheng, "Sound absorption of microperforated panels inside compact acoustic enclosures," *Journal of sound and vibration,* vol. 360, pp. 140-155, 2016.

[11] C. Yang, L. Cheng, and Z. Hu, "Reducing interior noise in a cylinder using micro-perforated panels," *Applied Acoustics,* vol. 95, pp. 50-56, 2015.

[12] K. Sakagami, I. Yamashita, M. Yairi, and M. Morimoto, "Sound absorption characteristics of a honeycomb-backed microperforated panel absorber: Revised theory and experimental validation," *Noise Control Engineering Journal,* vol. 58, no. 2, pp. 157-162, 2010.

[13] C. Wang, L. Cheng, J. Pan, and G. Yu, "Sound absorption of a micro-perforated panel backed by an irregular-shaped cavity," *The Journal of the Acoustical Society of America,* vol. 127, no. 1, pp. 238-246, 2010.

[14] F. Wu, Y. Xiao, D. Yu, H. Zhao, Y. Wang, and J. Wen, "Low-frequency sound absorption of hybrid absorber based on micro-perforated panel and coiled-up channels," *Applied Physics Letters,* vol. 114, no. 15, p. 151901, 2019.

[15] D. Kong, D. Xie, X. Tang, M. Hu, H. Xu, and Y. Qian, "Experimental study of a compact piezoelectric micro-perforated panel absorber with adjustable acoustic property," *The Journal of the Acoustical Society of America,* vol. 147, no. 3, pp. EL283-EL288, 2020.

[16] M. Q. Wu, "Micro-perforated panels for duct silencing," *Noise Control Engineering Journal,* vol. 45, no. 2, pp. 69-77, 1997.

[17] S. Allam and M. Åbom, "A new type of muffler based on microperforated tubes," *Journal of Vibration and Acoustics,* vol. 133, no. 3, p. 031005, 2011.

[18] M. Abom and S. Allam, "Dissipative silencers based on micro-perforated plates," SAE Technical Paper0148-7191, 2013.

[19] X. Wang, Y. Choy, and L. Cheng, "Hybrid noise control in a duct using a light micro-perforated plate," *The Journal of the Acoustical Society of America,* vol. 132, no. 6, pp. 3778-3787, 2012.

[20] X. Shi and C.-M. Mak, "Sound attenuation of a periodic array of micro-perforated tube mufflers," *Applied Acoustics,* vol. 115, pp. 15-22, 2017.

[21] X. Yu, L. Cheng, and X. You, "Hybrid silencers with micro-perforated panels and internal partitions," *Journal of the Acoustical Society of America,* vol. 137, no. 2, pp. 951-962, 2015.

[22] T. Bravo, C. Maury, and C. Pinhède, "Optimisation of micro-perforated cylindrical silencers in linear and nonlinear regimes," *Journal of Sound and Vibration,* vol. 363, pp. 359-379, 2016.

[23] D.-Y. Maa, "Potential of microperforated panel absorber," *the Journal of the*

Acoustical Society of America, vol. 104, no. 5, pp. 2861-2866, 1998.

[24] J. Liu and D. Herrin, "Enhancing micro-perforated panel attenuation by partitioning the adjoining cavity," *Applied Acoustics,* vol. 71, no. 2, pp. 120-127, 2010.

[25] X. Zhang and L. Cheng, "Acoustic impedance of micro-perforated panels in a grazing flow," *The Journal of the Acoustical Society of America,* vol. 145, no. 4, pp. 2461-2469, 2019.

[26] A. Selamet and Z. Ji, "Acoustic attenuation performance of circular expansion chambers with extended inlet/outlet," *Journal of Sound and Vibration,* vol. 223, no. 2, pp. 197-212, 1999.

[27] A. Selamet, F. Denia, and A. Besa, "Acoustic behavior of circular dual-chamber mufflers," *Journal of Sound and Vibration,* vol. 265, no. 5, pp. 967-985, 2003.

[28] M. Ouisse, L. Maxit, C. Cacciolati, and J.-L. Guyader, "Patch transfer functions as a tool to couple linear acoustic problems," *Journal of vibration and acoustics,* vol. 127, no. 5, pp. 458-466, 2005.

[29] J.-D. Chazot and J.-L. Guyader, "Prediction of transmission loss of double panels with a patch-mobility method," *The Journal of the Acoustical Society of America,* vol. 121, no. 1, pp. 267-278, 2007.

[30] M. Munjal and A. Doige, "Theory of a two source-location method for direct experimental evaluation of the four-pole parameters of an aeroacoustic element," *Journal of Sound and Vibration,* vol. 141, no. 2, pp. 323-333, 1990.

[31] C. Yang, L. Cheng, and J. Pan, "Absorption of oblique incidence sound by a

finite micro-perforated panel absorber," *The Journal of the Acoustical Society of America,* vol. 133, no. 1, pp. 201-209, 2013.